mathematics

Article

Study on a Quantitative Indicator for Surface Stability Evaluation of Limestone Strata with a Shallowly Buried Spherical Karst Cave

Peng Xie [1], Huchen Duan [1], Haijia Wen [2], Chao Yang [3,*], Shaokun Ma [4] and Zurun Yue [5]

1 College of Civil Engineering and Architecture, Hainan University, Haikou 570228, China; peng_xie@hainanu.edu.cn (P.X.); 21220856000146@hainanu.edu.cn (H.D.)
2 School of Civil Engineering, Chongqing University, Chongqing 400045, China; jhw@cqu.edu.cn
3 Key Laboratory of Geological Hazards on Three Gorges Reservoir Area (China Three Gorges University), Ministry of Education, No. 8 University Road, Yichang 443002, China
4 Guangxi Key Laboratory of Disaster Prevention and Engineering Safety, Guangxi University, Nanning 530004, China; mashaokun@gxu.edu.cn
5 State Key Laboratory of Mechanical Behavior and System Safety of Traffic Engineering Structures, Shijiazhuang Tiedao University, Shijiazhuang 050043, China; yzr@stdu.edu.cn
* Correspondence: yangchao0615@ctgu.edu.cn

Abstract: This paper developed a quantitative evaluation necessary to ensure ground stability, so a quantitative indicator (bearing capacity). A homogeneous axisymmetric model was generated, considering China's stress field and the Karst topography characteristics, simultaneously obtaining stress component expression. We then determined the bearing capacity calculation formula by combining the strength theory of shear failure and the stress component expressions. Finally, the comparison of the bearing capacity calculation results between theoretical analysis and a numerical simulation indicated that the error was less than 5%, and the result verified the rationality of the formula.

Keywords: ground stability; shallowly buried cave; quantitative evaluation; bearing capacity; love displacement function

MSC: 86-10; 83Bxx

check for updates

Citation: Xie, P.; Duan, H.; Wen, H.; Yang, C.; Ma, S.; Yue, Z. Study on a Quantitative Indicator for Surface Stability Evaluation of Limestone Strata with a Shallowly Buried Spherical Karst Cave. *Mathematics* **2022**, *10*, 2149. https://doi.org/10.3390/math10122149

Academic Editor: Manuel Pastor

Received: 5 May 2022
Accepted: 17 June 2022
Published: 20 June 2022

1. Introduction

In recent years, a series of strategies promoted the development of the regional economy, including the "Western Development Strategy", "the Belt and Road Initiatives", and so on [1]. As a result, the scale of infrastructure construction has dramatically increased in mantled Karst regions, and ground collapse has become a typical engineering problem [2,3]. To a certain extent, the number of ground collapse events decreased with the progress of control measures and science, but the economic loss increased [4,5]. Therefore, a quantitative evaluation of ground stability is essential to social security and engineering construction operations.

Bearing capacity is an important indicator to ensure the safety and stability of the limestone strata roof, which contains a shallowly buried Karst cave. To obtain an accurate bearing capacity calculation formula, a series of related studies have been made. They mainly focus on two aspects: elastic theoretical analysis and ultimate analysis [6]. In the process of elastic theoretical analysis, mathematical models are generated, including sheet models, beam models, rectangular plates, circular plates, and so on, and the stress component's formula was gained. For example, Goodier [7] and Howland et al. [8] generated a thin plate containing circular holes, and the inverse method was used to solve the problem. Considering the variety of Karst caves and the complexity of loading conditions, Xu et al. [9–11] performed a novel method and vision measurement system to monitor the component of stress. Taking into the spatial geometric characteristics of Karst caves, Xie et al. [12,13] provided an analytical solution which could represent the spatial characteristics of stress distribution around a shallow buried Karst cave containing fill materials in limestone strata. Furthermore, to ensure the stability of the strata roof containing a cave, the bear capacity of the strata roof was explored under different conditions. Zhao et al. [14] deduced stress distribution around the cave on the basis of elastic theory, and the stability of the rock foundation was analyzed. Xie et al. [15] also deduced stress distribution around the cave on the basis of elastic theory, and the stability of the rock foundation was analyzed. The limit equilibrium method includes the method of limit equilibrium, the slip line field method, and the upper and lower bound limit analysis method. The basic idea of ultimate analysis is to deduce the solution which meets both the yield condition and condition of equilibrium [16]. For example, the finite element limit analysis (FELA) was induced [17–20].

As mentioned above, many researched bearing capacities were obtained. Compared with the limit equilibrium method, theoretical analysis was the mathematical analysis method, and a general solution is much closer to field experimental conditions using the mechanical analysis method. Nevertheless, there is still some shortage. For example, the three-dimensional geometry characteristics of the strata neglected the effect of internal filling, and the technique was relatively singularly simple (complex function method). Therefore, considering limestone strata's spatial geometry and an interior filling of buried Karst caves, a bearing capacity formula was developed in this paper using the Love displacement function [21]. Firstly, considering China's stress field and the Karst topography characteristics, a homogeneous axisymmetric model was produced. Concurrently, stress component expressions were obtained. Then, combining the strength theory of shear failure and the stress component expressions, the bearing capacity formula was determined. Finally, to verify the rationality of the formula, a numerical simulation was performed using FLAC3D software. During the simulation process, horizontal constraints were applied to vertical boundaries. Moreover, the displacements of the bottom border were fixed in both the vertical and horizontal directions. The Mohr-Coulomb constitutive model was employed, and linear computation was used to solve the problem. In addition, the excavation of the void was performed. The comparison of the bearing capacity calculation results between theoretical analysis and a numerical simulation indicated that the error was less than 5%, so the research result would provide theoretical support for infrastructure construction in the mantled Karst region in China.

2. Theoretical Analysis of Spatial Stress Distribution

2.1. Mathematical Model and Boundary Conditions

2.1.1. Mathematical Model

Based on China's stress field and the Karst topography characteristics (Figure 1), a three-dimensional model was generated (Figure 2), and the cylindrical coordinates, as well as the spherical coordinates, were selected as the coordinate system (Figure 3). The basic assumptions are (a) the mathematical model was axisymmetric, (b) the spherical Karst cave was shallowly buried (h < 2.5 D) and the inner space was filled completely, and (c) the limestone strata were homogeneous, continuous, and isotropic.

The parameters in Figures 2 and 3 are

p_z—vertical stress caused by the external load;

p_0—horizontal stress surrounding the Karst cave caused by lateral earth pressure, $p_0 = k_0[p_z + \gamma(h + z)]$;

p_i—radial stress caused by internal fillings;

h—the vertical distance from the ground surface to the center of the sphere;

r—cylindrical radius;

R—the spherical Karst cave's radius, and R_1 is a certain constant for a case;

k_0—the coefficient of lateral earth pressure, $k_0 = \mu/(1-\mu)$, and μ is Poisson's ratio.

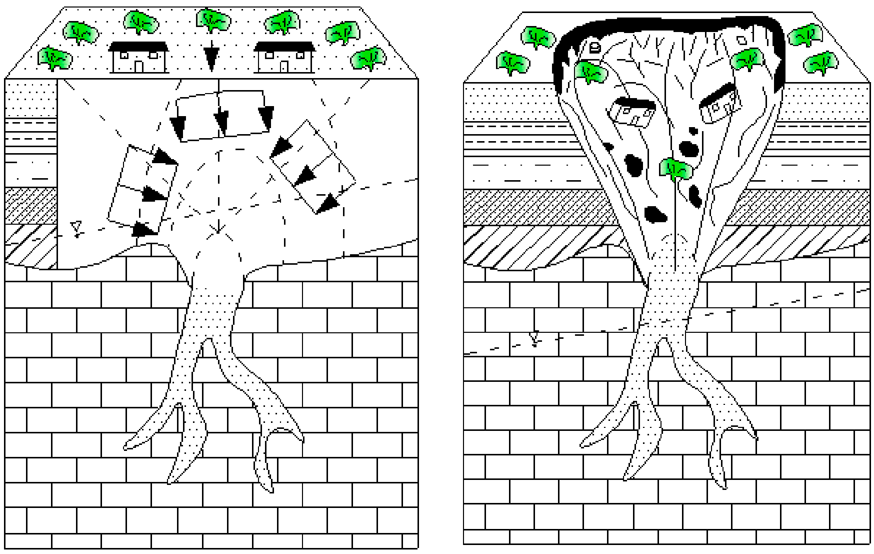

Figure 1. Limestone strata containing shallowly buried Karst caves. (**a**). Before collapse; (**b**). After collapse.

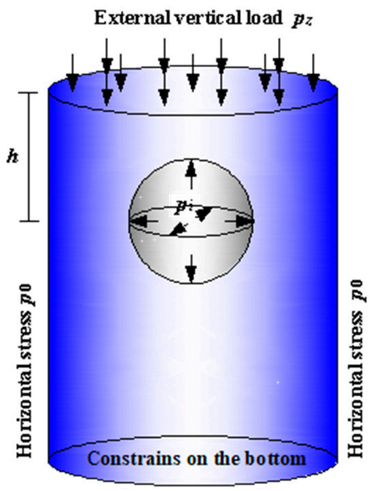

Figure 2. Sketch of limestone strata.

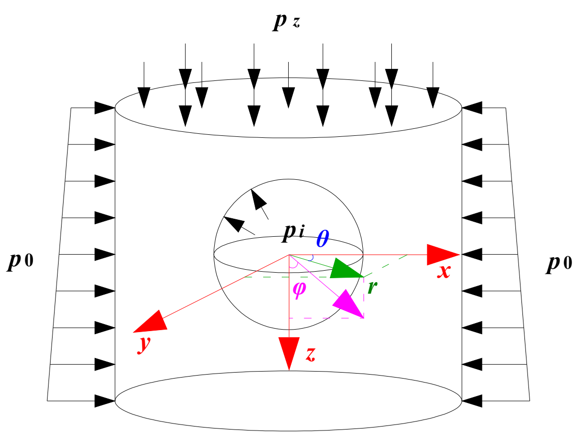

Figure 3. Mathematical model.

2.1.2. Boundary Conditions

(1) $z = -h, \sigma_z = p_z$;
(2) $r \to \infty, \sigma_r = [p_z + \gamma(h+z)]\mu/(1-\mu)$;
(3) $r \to \infty, \sigma_\theta = [p_z + \gamma(h+z)]\mu/(1-\mu)$;
(4) $R = R_1, \sigma_R = p_i$.

2.2. Theoretical Analysis

2.2.1. The Basic Theory

Considering the effect of gravity, the equilibrium differential equations are [21]

$$\left.\begin{array}{l} \frac{\partial\sigma_r}{\partial r} + \frac{\partial\tau_{zr}}{\partial z} + \frac{\sigma_r - \sigma_\theta}{r} = 0 \\ \frac{\partial\sigma_z}{\partial z} + \frac{\partial\tau_{zr}}{\partial r} + \frac{\tau_{zr}}{r} + \gamma = 0 \end{array}\right\} \tag{1}$$

Using the Love displacement method, the stress component's expressions are [21]

$$\left.\begin{array}{l} \sigma_r = \frac{\partial}{\partial z}(\mu\nabla^2 - \frac{\partial^2}{\partial r^2})\varphi(r,z) \\ \sigma_\theta = \frac{\partial}{\partial z}(\mu\nabla^2 - \frac{1}{r}\frac{\partial}{\partial r})\varphi(r,z) \\ \sigma_z = \frac{\partial}{\partial z}[(2-\mu)\nabla^2 - \frac{\partial^2}{\partial z^2}]\varphi(r,z) \\ \tau_{rz} = \frac{\partial}{\partial r}[(1-\mu)\nabla^2 - \frac{\partial^2}{\partial z^2}]\varphi(r,z) \end{array}\right\} \tag{2}$$

where ∇^2 is Laplace operator.

The transformation of the stress components' expression in different coordinates (between the spherical coordinate and cylindrical coordinate)

$$\left.\begin{array}{l} \sigma_R = \sigma_r \sin^2\varphi + \sigma_z \cos^2\varphi + 2\tau_{rz}\sin\varphi\cos\varphi \\ \sigma_\theta = \sigma_\theta \\ \sigma_\varphi = \sigma_r \cos^2\varphi + \sigma_z \sin^2\varphi - 2\tau_{rz}\sin\varphi\cos\varphi \\ \tau_{R\varphi} = (\sigma_r - \sigma_z)\sin\varphi\cos\varphi - \tau_{rz}(\sin^2\varphi - \cos^2\varphi) \end{array}\right\} \tag{3}$$

2.2.2. The General Solution

The Love displacement function (Equation (2)) generated in the spherical coordinate system [15,21] was

$$\varphi = A_1 r^4 + A_2 z^3 + A_3 z^2 r^2 + A_4 z r^2 + A_5 z R^{-1} \tag{4}$$

where, $A_i (i = 1, 2, 3, 4, 5)$ was the unknown coefficients.

Using the Love displacement function, the stress components are

$$\sigma_r = 4[(2\mu-1)A_3]z + 2[3\mu A_2 + (2\mu-1)A_4] + A_5[15r^2z^2R^{-7} + 3(2\mu-1)z^2R^{-5} - 3r^2R^{-5} + (1-2\mu)R^{-3}] \tag{5}$$

$$\sigma_\theta = 4[(2\mu-1)A_3]z + 2[3\mu A_2 + (2\mu-1)A_4] + A_5[3(2\mu-1)z^2R^{-5} + (1-2\mu)R^{-3}] \tag{6}$$

$$\sigma_z = 8[(2-\mu)A_3]z + 2[3(1-\mu)A_1 + 2(2-\mu)A_3] + A_4[15z^4R^{-7} - 6(1+\mu)z^2R^{-5} + (2\mu-1)R^{-3}] \tag{7}$$

$$\tau_{rz} = 4[8(1-\mu)A_1 - \mu A_3]r + A_5[15rz^3R^{-7} - 3(1+2\mu)rzR^{-5}] \tag{8}$$

In spherical coordinates, the stress components were

$$\begin{array}{l} \sigma_R = \{4[16(1-\mu)A_1 - A_3]\sin^2\varphi\cos\varphi + 8[(2-\mu)A_3]\cos^3\varphi\}R + \{2[3\mu A_2 + (2\mu-1)A_4]\sin^2\varphi + \\ \quad 2[3(1-\mu)A_2 + 2(2-\mu)A_4]\cos^2\varphi\} + A_5[15\cos^6\varphi + 15\sin^4\varphi\cos^2\varphi + 30\sin^2\varphi\cos^4\varphi - 3\sin^4\varphi - \\ 6(1+\mu)\cos^4\varphi - 3(3+2\mu)\sin^2\varphi\cos^2\varphi + (1-2\mu)\sin^2\varphi + (2\mu-1)\cos^2\varphi]\frac{1}{R^3} \end{array} \tag{9}$$

$$\sigma_\theta = \{4[(2\mu-1)A_3]\cos\varphi\}R + 2[3\mu A_2 + (2\mu-1)A_4]A_5[3(2\mu-1)\cos^2\varphi + (1-2\mu)]\frac{1}{R^3} \tag{10}$$

$$\sigma_\varphi = \{4[(2\mu-1)A_3\cos^3\varphi + 8[-8(1-\mu)A_1 + 2A_3]\sin^2\varphi\cos\varphi\}R + \{2[3\mu A_2 + (2\mu-1)A_4]\cos^2\varphi + 2[3(1-\mu)A_2 + 2(2-\mu)A_4]\sin^2\varphi\} + A_5[3(2\mu-1)\cos^2\varphi + (1-2\mu)(\cos^2\varphi - \sin^2\varphi)]\frac{1}{R^3} \tag{11}$$

$$\tau_{R\varphi} = \{4[8(1-\mu)A_1 + (3\mu-5)A_3]\sin^2\varphi\cos^2\varphi - 4[8(1-\mu)A_1 - \mu A_3]\sin^3\varphi\}R + [6(2\mu-1)A_2 + 2(4\mu-5A_4]\sin\varphi\cos\varphi + 2A_5(1+\mu)\frac{1}{R^3}\sin\varphi\cos\varphi \tag{12}$$

Equation (1) is satisfied, so

$$8A_1 + 2A_3 = \frac{\gamma}{8(\mu-1)} \tag{13}$$

Using boundary condition (1)

$$-8[(2-\mu)A_3]h + 2[3(1-\mu)A_2 + 2(2-\mu)A_4] - A_5\frac{1}{h^3}[15\cos^7\varphi - 6(1+\mu)\cos^5\varphi + (2\mu-1)\cos^3\varphi] = p_z \tag{14}$$

Using boundary conditions (2) and (3), respectively

$$4(2\mu-1)A_3 = \frac{\mu}{1-\mu}\gamma \tag{15}$$

$$6\mu A_2 + 2(2\mu-1)A_4 = \frac{\mu}{1-\mu}(p_z + \gamma h) \tag{16}$$

Combining boundary condition (4) with Equation (9)

$$\{4[16(1-\mu)A_2 - A_4]\sin^2\varphi\cos\varphi + 8[(2-\mu)A_4]\cos^3\varphi\}R_1 + \{2[3\mu A_3 + (2\mu-1)A_5]\sin^2\varphi + 2[3(1-\mu)A_3 + (2-\mu)A_5]\cos^2\varphi\} + A_9[15\cos^6\varphi + 15\sin^4\varphi\cos^2\varphi + 30\sin^2\varphi\cos^4\varphi - 3\sin^4\varphi - 6(1+\mu)\cos^4\varphi - 3(3+2\mu)\sin^2\varphi\cos^2\varphi + (1-2\mu)\sin^2\varphi + (2\mu-1)\cos^2\varphi]\frac{1}{{R_1}^3} = p_i \tag{17}$$

Combining Equations (13)–(17), the equations of the stress components are

$$\sigma_R = \{4[16(1-\mu)A_1 - A_3]\sin^2\varphi\cos\varphi + 8[(2-\mu)A_3]\cos^3\varphi\}R + \{2[3\mu A_2 + (2\mu-1)A_4]\sin^2\varphi + 2[3(1-\mu)A_2 + 2(2-\mu)A_4]\cos^2\varphi\} + A_5[15\cos^6\varphi + 15\sin^4\varphi\cos^2\varphi + 30\sin^2\varphi\cos^4\varphi - 3\sin^4\varphi - 6(1+\mu)\cos^4\varphi - 3(3+2\mu)\sin^2\varphi\cos^2\varphi + (1-2\mu)\sin^2\varphi + (2\mu-1)\cos^2\varphi]\frac{1}{R^3} \tag{18}$$

$$\sigma_\theta = \{4[(2\mu-1)A_3]\cos\varphi\}R + 2[3\mu A_2 + (2\mu-1)A_4] + A_5[3(2\mu-1)\cos^2\varphi + (1-2\mu)]\frac{1}{R^3} \tag{19}$$

$$\sigma_\varphi = \{4[(2\mu-1)A_3\cos^3\varphi + 8[-8(1-\mu)A_1 + 2A_3]\sin^2\varphi\cos\varphi\}R + \{2[3\mu A_2 + (2\mu-1)A_4]\cos^2\varphi + 2[3(1-\mu)A_2 + 2(2-\mu)A_4]\sin^2\varphi\} + A_5[3(2\mu-1)\cos^2\varphi + (1-2\mu)(\cos^2\varphi - \sin^2\varphi)]\frac{1}{R^3} \tag{20}$$

$$\tau_{R\varphi} = \{4[8(1-\mu)A_1 + (3\mu-5)A_3]\sin^2\varphi\cos^2\varphi - 4[8(1-\mu)A_1 - \mu A_3]\sin^3\varphi\}R + [6(2\mu-1)A_2 + 2(4\mu-5)A_4]\sin\varphi\cos\varphi + 2A_5(1+\mu)\frac{1}{R^3}\sin\varphi\cos\varphi \tag{21}$$

where

$$A_1 = \frac{(6\mu-1)}{64(1-\mu)(1-2\mu)}\gamma,\ A_2 = -\frac{B_1}{6B_2},\ A_3 = \frac{\mu\gamma}{4(1-\mu)(2\mu-1)},\ A_4 = -\frac{B_3}{2B_2},\ A_5 = -\frac{B_4}{B_2}$$

$$B_1 = 2(2\mu-1)h^3[(1-\mu)(2\mu-1)p_z + 2\mu(2-\mu)\cos^2\varphi] - \mu(2\mu-1){R_1}^3(p_z+\gamma h)[2(2-\mu)\cos^2\varphi + (2\mu-1)\sin^2\varphi][15\cos^7\varphi - 6(1+\mu)\cos^5\varphi + (2\mu-1)\cos^3\varphi] - 4\mu h^3(2-\mu)(2\mu-1)(p_z + \gamma h)[2(2-\mu)\cos^2\varphi - (1+\mu)\sin^2\varphi] + (2\mu-1){R_1}^3[15\cos^7\varphi - 6(1+\mu)\cos^5\varphi + (2\mu-1)\cos^3\varphi][(1-\mu)(2\mu-1)p_i + (6\mu-1)(1-\mu)\gamma R_1\sin^2\varphi\cos\varphi - 2(2-\mu)R_1\gamma\cos^3\varphi + \mu R_1\gamma\sin^2\varphi\cos\varphi]$$

$B_2 = (1-\mu)(2\mu-1)\{R_1{}^3(1-2\mu)[\mu\sin^2\varphi + (1-\mu)\cos^2\varphi][15\cos 7\varphi - 6(1+\mu)\cos^5\varphi + (2\mu-1)$
$\cos^3\varphi] + R_1{}^3\mu[2(2-\mu)\cos^2\varphi + (2\mu-1)\sin^2\varphi][15\cos^7\varphi - 6(1+\mu)\cos^5\varphi + (2\mu-1)\cos^3\varphi]$
$+4\mu h^3(2-\mu)[2(2-\mu)\cos^2\varphi - (1+\mu)\sin^2\varphi] + 2h^3(1-\mu)(1-2\mu)[2(2-\mu)\cos^2\varphi - (1+\mu)\sin^2\varphi]\}$
$B_3 = -2\mu h^3[(1-\mu)(2\mu-1)p_z + 2\mu(2-\mu)\gamma h][2(2-\mu)\cos^2\varphi - (1+\mu)\sin^2\varphi] + \mu(2\mu-1)R_1{}^3$
$(p_z+\gamma h)[\mu\sin^2\varphi + (1-\mu)\cos^2\varphi][15\cos^7\varphi - 6(1+\mu)\cos^5\varphi + (2\mu-1)\cos^3\varphi] + 2\mu h^3(1-\mu)$
$(2\mu - 1(p_z+\gamma h)[2(2-\mu)\cos^2\varphi - (1+\mu)\sin^2\varphi] - \mu[15\cos^7\varphi - 6(1+\mu)\cos^5\varphi + (2\mu-1)\cos^3\varphi]$
$[(1+\mu)(2\mu-1)R_1{}^3p_i + (6\mu-1)(1-\mu)R_1{}^4\gamma\cos^3\varphi + \mu R_1{}^4\gamma\sin^2\varphi\cos\varphi]$
$B_4 = h^3\{(1-\mu)R_1{}^3[(1-\mu)(2\mu-1)p_z + 2\mu(2-\mu)\gamma h][\mu\sin^2\varphi + (1-\mu)\cos^2\varphi] + \gamma R_1{}^3[(1-\mu)(2\mu p_z +$
$2\mu(2-\mu)\gamma h][2(2-\mu)\cos^2\varphi + (2\mu-1)\sin^2\varphi] + 2\mu(2-\mu)(2\mu-1)R_1{}^3(p_z+\gamma h)[\mu\sin^2 +$
$(1-\mu)\cos^2\varphi] - \mu(1-\mu)(2\mu-1)R_1{}^3(p_z+\gamma h)[2(2-\mu)\cos^2\varphi + (2\mu-1)\sin^2\varphi] - 2\mu$
$(2-R_1{}^3[(1-\mu)(2\mu-1)p_i + (6\mu-1)(1-\mu)\gamma R_1\sin^2\varphi\cos\varphi - 2(2-\mu)R_1\gamma\cos^3\varphi +$
$\mu R_1\gamma\sin^2\varphi\cos\varphi] + (1-\mu)(2\mu-1)R_1{}^3[(1-\mu)(2\mu-1)p_i + (6\mu-1)(1-\mu)\gamma R_1\sin^2\varphi\cos\varphi -$
$2(2-\mu)R_1\gamma\cos^3\varphi + \mu R_1\gamma\sin^2\varphi\cos\varphi]\}$

3. Bearing Capacity of Limestone Strata Roof

3.1. Failure Mechanism of Ground Collapse

In general, soil arch theory explains ground collapse. Figure 4 shows that the vertical pressure of the roof increases due to the influence of external vertical load and gravity. Concurrently, a radical shear zone appears. Furthermore, rock mass in high the pressure-zone expands laterally to low-pressure areas. Eventually, collapse formed along sliding surfaces (AB, CD) (Figure 3).

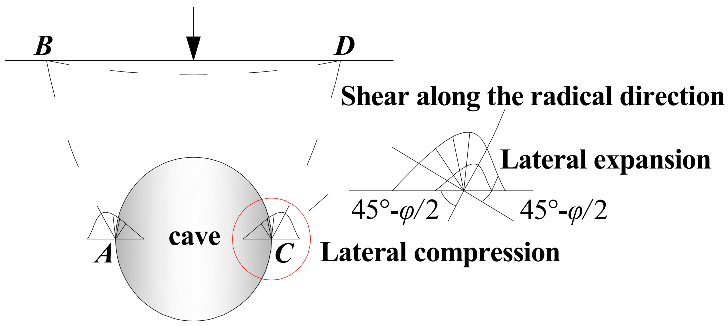

Figure 4. Vertical cross-section of limestone strata containing the spherical Karst cave, which was affected by the vertical load.

3.2. Theoretical Analysis of Bearing Capacity

3.2.1. The Basic Theory

Mohr-Coulomb Strength Theory

O. Maurs (1910) proposed that the failure of materials is the shear strength of the material (Figure 5).

When a micro-unit is taken (Figure 6), the limit equilibrium condition of the material can be obtained (Equation (22) or Equation (23)).

$$\sigma_1 = \sigma_3\tan^2(45^\circ + \frac{\varphi_1}{2}) + 2c\tan(45^\circ + \frac{\varphi_1}{2}) \tag{22}$$

$$\sigma_3 = \sigma_1\tan^2(45^\circ - \frac{\varphi_1}{2}) - 2c\tan(45^\circ - \frac{\varphi_1}{2}) \tag{23}$$

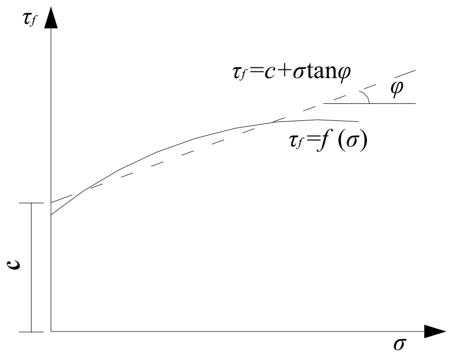

Figure 5. Mohr envelope.

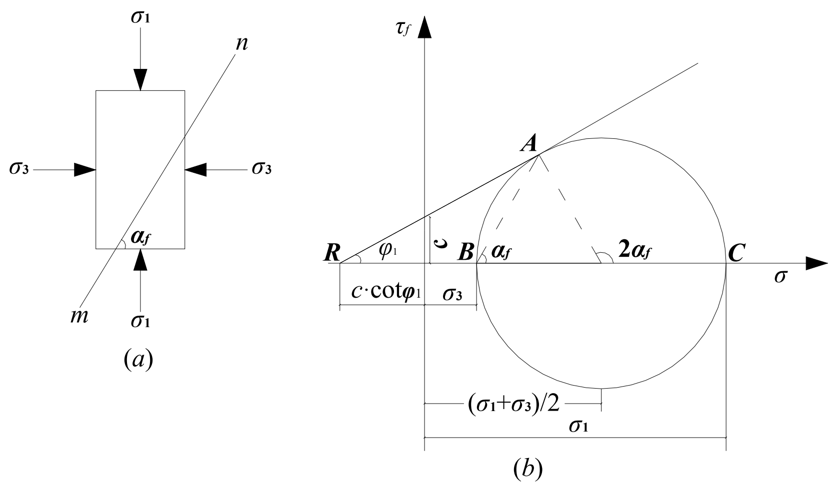

Figure 6. Mohr's circle when any point of the material reaches equilibrium state (**a**) microelement, (**b**) Mohr's circle.

Principle Stress of Any Point

Principle stress of any point calculated using the Equation

$$\sigma^3 - I_1\sigma^2 + I_2\sigma - I_3 = 0$$

where

$$I_1 = \sigma_{11} + \sigma_{22} + \sigma_{33} = \sigma_x + \sigma_y + \sigma_z$$

$$I_2 = \begin{vmatrix} \sigma_{22} & \sigma_{23} \\ \sigma_{32} & \sigma_{33} \end{vmatrix} + \begin{vmatrix} \sigma_{11} & \sigma_{13} \\ \sigma_{31} & \sigma_{33} \end{vmatrix} + \begin{vmatrix} \sigma_{11} & \sigma_{12} \\ \sigma_{21} & \sigma_{22} \end{vmatrix} = \begin{vmatrix} \sigma_y & \tau_{yz} \\ \sigma_{zy} & \sigma_z \end{vmatrix} + \begin{vmatrix} \sigma_x & \tau_{xz} \\ \tau_{zx} & \sigma_z \end{vmatrix} + \begin{vmatrix} \sigma_x & \sigma_{xy} \\ \sigma_{yx} & \sigma_y \end{vmatrix}$$

$$I_3 = \begin{vmatrix} \sigma_{11} & \sigma_{12} & \sigma_{13} \\ \sigma_{21} & \sigma_{22} & \sigma_{23} \\ \sigma_{31} & \sigma_{32} & \sigma_{33} \end{vmatrix} = \begin{vmatrix} \sigma_x & \tau_{xy} & \tau_{xz} \\ \tau_{yx} & \sigma_y & \tau_{yz} \\ \tau_{zx} & \tau_{zy} & \sigma_z \end{vmatrix}$$

Transformation of Stress Components in Different Coordinate Systems

According to the relationship among different coordinate systems (Figure 7), a transformation of stress components in various coordinate systems are

$$\sigma_c = [\beta_c][\sigma_d][\beta_c]^T \tag{24}$$

$$\sigma_s = [\beta_s][\sigma_d][\beta_s]^T \tag{25}$$

where

$$\sigma_d = \begin{bmatrix} \sigma_x & \tau_{yx} & \tau_{zx} \\ \tau_{xy} & \sigma_y & \tau_{yz} \\ \tau_{xz} & \tau_{yz} & \sigma_z \end{bmatrix} \sigma_c = \begin{bmatrix} \sigma_r & \tau_{\theta r} & \tau_{zr} \\ \tau_{r\theta} & \sigma_\theta & \tau_{z\theta} \\ \tau_{rz} & \tau_{\theta z} & \sigma_z \end{bmatrix} \sigma_s = \begin{bmatrix} \sigma_R & \tau_{\theta R} & \tau_{R\varphi} \\ \tau_{R\theta} & \sigma_\theta & \tau_{\varphi\theta} \\ \tau_{R\varphi} & \tau_{\theta\varphi} & \sigma_\varphi \end{bmatrix}$$

$$\beta_c = \begin{bmatrix} \cos\theta & \sin\theta & 0 \\ -\sin\theta & \cos\theta & 0 \\ 0 & 0 & 1 \end{bmatrix} \beta_s = \begin{bmatrix} \cos\theta\sin\varphi & \sin\theta\sin\varphi & \cos\varphi \\ \cos\theta\cos\varphi & \sin\theta\cos\varphi & -\sin\varphi \\ -\sin\varphi & \cos\varphi & 0 \end{bmatrix}$$

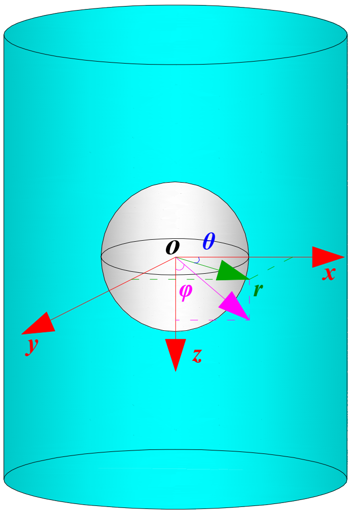

Figure 7. Sketch of relationship among different coordinates.

3.3. General Solution of Bearing Capacity Calculation Formula

Based on the explanation in the Section 3.1, shear failure was caused by ground collapse, which was generated from points A and C. The shear failure of points A and C was determined as the basis of ground instability, and Mohr-Coulomb strength theory was the shear failure criteria.

According to Equations (18)–(21), stress components of points A and C are

$$\sigma_R = p_i \tag{26}$$

$$\sigma_\theta = \frac{3\mu}{2(1+\mu)(1-\mu)} p_z + \frac{3\mu\gamma}{2(1+\mu)(1-\mu)} h - \frac{(1-2\mu)}{2(1+\mu)} p_i \tag{27}$$

$$\sigma_\varphi = \frac{(2-\mu)}{2(1+\mu)(1-\mu)} p_z + \frac{9\mu\gamma}{2(1+\mu)(1-\mu)(2\mu-1)} h + \frac{(1-2\mu)}{2(1+\mu)} p_i \tag{28}$$

$$\tau_{R\varphi} = \frac{(6\mu-1)}{2(2\mu-1)} \gamma R_1 + \frac{\mu^2}{(1-\mu)(2\mu-1)} \gamma R_1 \tag{29}$$

Therefore

$$\sigma^3 - I_1\sigma^2 + I_2\sigma - I_3 = 0 \tag{30}$$

where

$$I_1 = \frac{1}{1-\mu} p_z + \frac{3\mu\gamma}{(1-\mu)(2\mu-1)} h + p_i I_2 = \frac{3\mu(2-\mu)}{4(1+\mu)^2(1-\mu)^2} {p_z}^2 - \frac{(2\mu^2-8\mu-1)p_i}{2(1+\mu)^2(1-\mu)} p_z - \frac{3\mu\gamma(\mu^2-7\mu+1)}{2(1+\mu)^2(1-\mu)^2(2\mu-1)} p_z h + \frac{27\mu^2\gamma^2}{4(1+\mu)^2(1-\mu)^2(2\mu-1)} h^2 + \frac{27\mu^2\gamma p_i}{2(1+\mu)^2(1-\mu)(2\mu-1)} h - \frac{(1-2\mu)^2}{4(1+\mu)^2} {p_i}^2 - [\frac{3\mu}{2\mu-1}\gamma R_1 - \frac{1}{2(2\mu-1)}\gamma R_1 + \frac{\mu^2}{(1-\mu)(2\mu-1)}\gamma R_1]^2 I_3 = 0$$

So

$$\sigma_1 = \frac{I_1 + \sqrt{I_1{}^2 - 4I_2}}{2}\sigma_3 = 0$$

where

$$I_1 = \tfrac{1}{1-\mu}p_z + \tfrac{3\mu\gamma}{(1-\mu)(2\mu-1)}h + p_i$$
$$I_2 = \tfrac{3\mu(2-\mu)}{4(1+\mu)^2(1-\mu)^2}p_z{}^2 - \tfrac{(2\mu^2-8\mu-1)p_i}{2(1+\mu)^2(1-\mu)}p_z - \tfrac{3\mu\gamma(\mu^2-7\mu+1)}{2(1+\mu)^2(1-\mu)^2(2\mu-1)}p_z h +$$
$$\tfrac{27\mu^2\gamma^2}{4(1+\mu)^2(1-\mu)^2(2\mu-1)}h^2 + \tfrac{27\mu^2\gamma p_i}{2(1+\mu)^2(1-\mu)(2\mu-1)}h - \tfrac{(1-2\mu)^2}{4(1+\mu)^2}p_i{}^2 -$$
$$[\tfrac{3\mu}{2\mu-1}\gamma R_1 - \tfrac{1}{2(2\mu-1)}\gamma R_1 + \tfrac{\mu^2}{(1-\mu)(2\mu-1)}\gamma R_1]^2$$
$$I_3 = 0$$

Combing Equations (26)–(30) with Equation (22)

$$\begin{aligned}
&\tfrac{3\mu(2-\mu)}{(1+\mu)^2(1-\mu)^2}p_z{}^2 - [\tfrac{2(2\mu^2-8\mu-1)}{(1+\mu)^2(1-\mu)}p_i + \tfrac{6\mu\gamma h(\mu^2-7\mu+1)}{(1+\mu)^2(1-\mu)^2(2\mu-1)} \\
&+\tfrac{8}{1-\mu}c'\tan(\tfrac{\pi}{4}+\tfrac{\varphi_1}{2})]p_z + \tfrac{27\mu^2\gamma^2}{(1+\mu)^2(1-\mu)^2(2\mu-1)}h^2 + \tfrac{54\mu^2\gamma p_i}{(1+\mu)^2(1-\mu)(2\mu-1)}h \\
&-\tfrac{(1-2\mu)^2}{(1+\mu)^2}p_i{}^2 - 4[\gamma R_1\tfrac{6\mu-1}{2(2\mu-1)} + \tfrac{\mu^2}{(1-\mu)(2\mu-1)}\gamma R_1]^2 - \tfrac{24\mu\gamma}{(1-\mu)(2\mu-1)}hc\tan(\tfrac{\pi}{4}+\tfrac{\varphi_1}{2}) \\
&-8p_i c\tan(\tfrac{\pi}{4}+\tfrac{\varphi_1}{2}) + 16c^2\tan^2(\tfrac{\pi}{4}+\tfrac{\varphi_1}{2}) = 0
\end{aligned} \tag{31}$$

So

$$p_{z1} = \frac{M_2 + \sqrt{M_2{}^2 - 4M_1M_3}}{2M_1} \tag{32}$$

$$p_{z2} = \frac{M_2 - \sqrt{M_2{}^2 - 4M_1M_3}}{2M_1} \tag{33}$$

where $M_1 = \frac{3\mu(2-\mu)}{(1+\mu)^2(1-\mu)^2}$

$$M_2 = \tfrac{2(2\mu^2-8\mu-1)}{(1+\mu)^2(1-\mu)}p_i + \tfrac{6\mu\gamma h(\mu^2-7\mu+1)}{(1+\mu)^2(1-\mu)^2(2\mu-1)} + \tfrac{8}{1-\mu}c\tan(\tfrac{\pi}{4}+\tfrac{\varphi_1}{2})\cdot\tfrac{1}{(2\mu-1)} -$$
$$M_3 = \tfrac{27\mu^2\gamma^2h^2}{(1+\mu)^2(1-\mu)^2(2\mu-1)} + \tfrac{54\mu^2\gamma h p_i}{(1+\mu)^2(1-\mu)}\cdot\tfrac{1}{(2\mu-1)} - \tfrac{(1-2\mu)^2}{(1+\mu)^2}p_i{}^2 - 4[\tfrac{\gamma R_1(6\mu-1)}{2(2\mu-1)} -$$
$$\tfrac{24\mu\gamma hc}{(2\mu-1)}\tfrac{1}{(1-\mu)}\tan(\tfrac{\pi}{4}+\tfrac{\varphi_1}{2}) - 8p_i c\tan(\tfrac{\pi}{4}+\tfrac{\varphi_1}{2}) +$$
$$16c^2\tan^2(\tfrac{\pi}{4}+\tfrac{\varphi_1}{2}) + 16c^2\tan^2(\tfrac{\pi}{4}+\tfrac{\varphi_1}{2})$$

Among p_{z1} and p_{z2}, the positive value and the smaller one is the solution.

4. Application and Validation Test

We performed a numerical simulation to validate the rationality of the bearing capacity calculation formula. According to the site investigation, the numerical simulation model was generated (Figure 8). The number of elements for the entire calculation model was 2496, and the spatial geometry parameter and the attribute parameter are as in Table 1. During the simulation process, horizontal constraints were applied to vertical boundaries. Moreover, the displacements of the bottom border were fixed in both the vertical and horizontal directions. The Mohr-Coulomb constitutive model was employed, and linear computation was used to solve the problem. In addition, the excavation of the void was performed. Finally, the vertical load was applied step-by-step from 2 MPa to 38 MPa at an interval of 2 MPa, and the vertical subsidence of point B was monitored (Figure 9, Table 2).

Figure 10 is the P-S curve using monitoring data (B point in Figure 9), which shows the relationship between vertical load and vertical subsidence. When the applied vertical load reaches 36 MPa (red point in Figure 10), the small change of vertical load will bring a sudden shift of vertical subsidence. So, the value of 36 MPa is the value of the bearing capacity. In addition, the value of the bearing capacity is 37.94 MPa using the bearing capacity calculation formula. A value comparison indicates that the error is less than 5%, and the results verified the rationality of the formula.

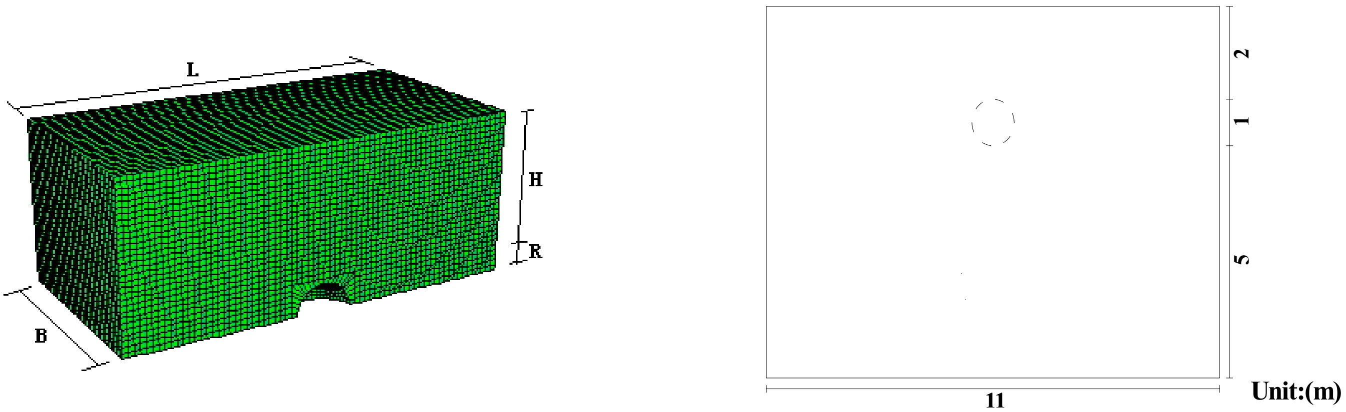

(a) (b)

Figure 8. Sketch of numerical simulation model. (**a**) 1/4 geometry model, and mesh; (**b**) The dimensions of numerical simulation model.

Table 1. The spatial geometry parameter and the attribute parameter.

Parameters / Materials	γ (kN/m^3)	E (GPa)	c (MPa)	φ (°)	μ	R_1 (m)	p_z (KPa)	p_i (KPa)	h (m)
Limestone strata	26,500	35	7.8	42.3	0.25	0.5	0	0	2

(a) (b)

Figure 9. Sketch of monitored point layout. (**a**) vertical cross-section; (**b**) horizontal cross-section.

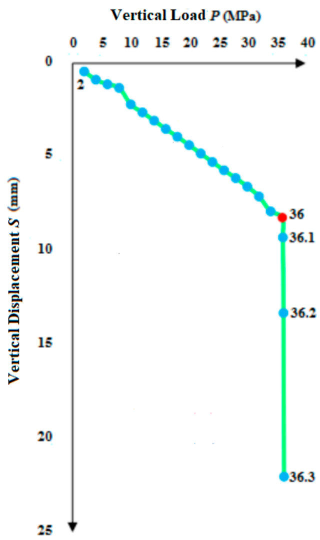

Figure 10. P-S curve is the fitting result of the numerical result in Table 2, and the red point is a sudden shift of vertical subsidence.

Table 2. Applied load and corresponding subside of the critical point.

Serial Number	External Vertical *P* (MPa)	Subsidence *S* (mm)
1	2	0.437865
2	4	0.874118
3	6	1.12011
4	8	1.3118
5	10	2.19316
6	12	2.61823
7	14	3.05638
8	16	3.5
9	18	3.91891
10	20	4.36046
11	22	4.80857
12	24	5.2625
13	26	5.7035
14	28	6.1208
15	30	6.5762
16	32	7.10112
17	34	7.89486
18	36	8.22704
19	36.1	9.28338
20	36.2	13.3104
21	36.3	22.0348

5. Discussion

5.1. Bearing Capacity Change Caused by Various Factors

The diagrams were drawn to study the effect of different influencing factors (Figure 11). Bearing capacity values increase with the increase in parameters, including γ (unit weight), c (cohesion strength), φ_1 (internal friction angle), μ (Poisson's ratio), and h (the vertical distance from the ground surface to the center of the sphere). However, the curve has a reverse trend for R (the spherical Karst cave's internal radius). In addition, the effect of p_i (radial stress caused by fill materials) was neglected. Nevertheless, the trend of value change suggests that the bearing capacity calculation formula is reasonable [17–20].

5.2. General Solution of Stress Components

An accurate general solution of stress components is the precondition to obtaining the rational bearing capacity calculation formula. Figure 12 presents the general solution of stress components that could reflect the spatial distribution characteristic surrounding a Karst cave, but still, there is an error (the maximum value is not more than 5.0%). To improve the accuracy of the general solution, further research performed on these three aspects is needed: (1) increasing the type of displacement function component; (2) introducing various analysis methods; (3) using a non-linear constitutive model.

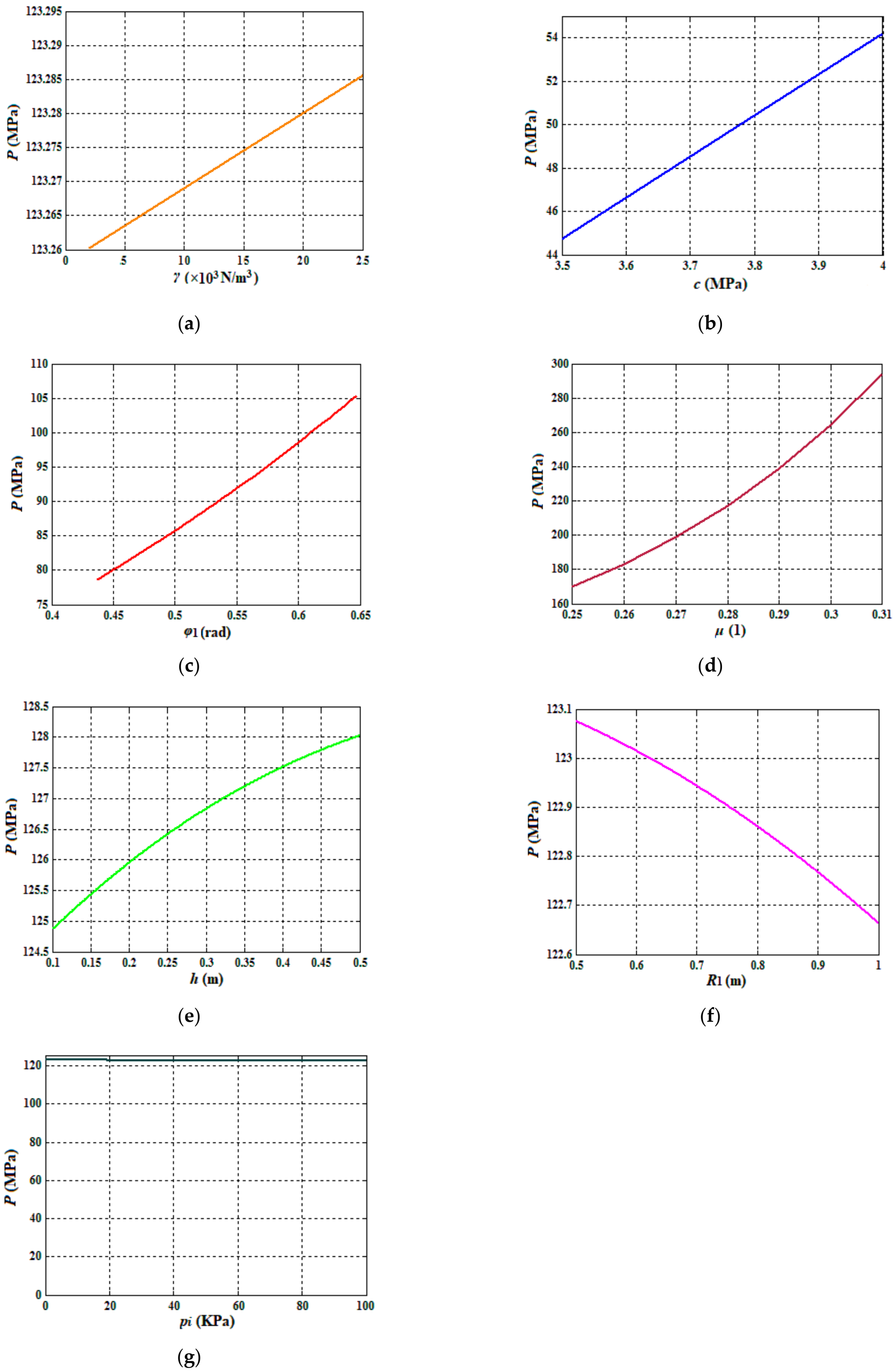

Figure 11. The curves of the bear capacity of limestone strata caused by a single influencing factor. (**a**) The range of γ value is from 2 kN/m^3 to 4 MPa. (**b**) The range of c value is from 3.5 MPa to 25 kN/m^3. (**c**) The range of φ_1 value is from 0.43 rad to 0.63 rad (**d**) The range of μ value is from 0.25 to 0.31. (**e**) The range of h value is from 0.1 m to 0.5 m (**f**) The range of R_1 value is from 0.5 m to 1.0 m. (**g**) The range of p_i value is from 0 kPa to 100 kPa.

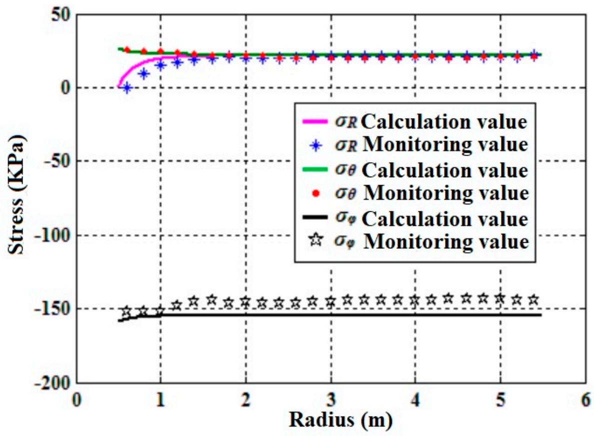

Figure 12. A value comparison.

6. Conclusions

The generated homogeneous axisymmetric model was based on China's stress field and the Karst topography characteristics. Meanwhile, we obtained the stress component expressions.

Combing the strength theory of shear failure and the stress components surrounding the Karst cave, the limestone strata roof's bearing capacity calculation formula is determined, containing a shallowly buried spherical Karst cave. Bearing capacity values increase with the increase in parameters, including γ (unit weight), c (cohesion strength), φ_1 (internal friction angle), μ (Poisson's ratio), and h (the vertical distance from the ground surface to the center of the sphere). However, the curve has a reverse trend for R (the spherical Karst cave's internal radius). In addition, the effect of p_i (radial stress caused by fill materials) was neglected. Nevertheless, the trend of value change suggests that the bearing capacity calculation formula is reasonable.

A value comparison indicated the maximum error was less than 5% between theoretical calculation and numerical simulation, and the result verified the rationality of the bearing capacity calculation formula. To improve the accuracy of the general solution, further research performed on these three aspects is needed: (1) increasing the type of displacement function component; (2) introducing various analysis methods; (3) using a non-linear constitutive model.

Author Contributions: Conceptualization, C.Y.; methodology, P.X. and H.W.; software, P.X.; validation, P.X. and H.D.; formal analysis, P.X. and H.D.; investigation, Z.Y.; resources, Z.Y.; data curation, H.D.; writing—original draft preparation, P.X.; writing—review and editing, H.W.; supervision, C.Y. and H.W.; project administration, Z.Y.; funding acquisition, P.X.; Z.Y. and S.M. All authors have read and agreed to the published version of the manuscript.

Funding: The research on which this article is based has been supported by grants: The Systematic Project of Key Laboratory of Geological Hazards on Three Gorges Reservoir Area (China Three Gorges University), Ministry of Education (No. 2020KDZ04); Hainan Provincial Natural Science Foundation of China (Grant No: 422RC599, 520QN229, 122RC541); The Systematic Project of State Key Laboratory of Mechanical Behavior and System Safety of Traffic Engineering Structures, Shijiazhuang Tiedao University (Grant No: KF2022-03); the Scientific Research Startup Foundation of Hainan University (Grant No: KYQD(2R)1969); National Natural Science Foundation of China (42002293); and National Natural Science Foundation of China (52068019).

Institutional Review Board Statement: Not applicable.

Informed Consent Statement: Not applicable.

Conflicts of Interest: The authors declare no conflict of interest.

References

1. Xie, P.; Wen, H.J.; Zhang, Y.Y.; Zhang, X.X.; Hu, J. A method for identification and reconstruction of hard structural planes, weak interlayer, and cavities in the limestone near surface. *Eur. J. Environ. Civ. Eng.* **2020**, *24*, 2489–2511. [CrossRef]
2. Gutierrez, F.; Parise, M.; Dewaele, J.; Jourde, H. A review on natural and human-induced geohazards and impacts in karst. *Earth-Sci. Rev.* **2014**, *138*, 61–88. [CrossRef]
3. Xie, P.; Wen, H.; Xiao, P.; Zhang, Y. Evaluation of ground-penetrating radar (GPR) and geology survey for slope stability study in mantled karst region. *Environ. Earth Sci.* **2018**, *77*, 122. [CrossRef]
4. Xiao, X.X.; Gutiérrez, F.; Guerrero, J. The impact of groundwater drawdown and vacuum pressure on sinkhole development. Physical laboratory models. *Eng. Geol.* **2020**, *279*, 105894. [CrossRef]
5. Wang, X.L.; Lai, J.X.; He, S.Y.; Garnes, R.S.; Zhang, Y.W. Karst geology and mitigation measures for hazards during metro system construction in Wuhan, China. *Nat. Hazards* **2020**, *103*, 2905–2927. [CrossRef]
6. Yin, J.F.; Lei, Y.; Chen, Q.N. Summary about researches on the calculation method for the bearing capacity of cave roof. *J. Hunan Univ. Arts Sci.* **2017**, *29*, 68–72. (In Chinese)
7. Goodier, J.N. Concentrations of stress around spheroidal and cylindrical inclusions and flaws. *Trans. ASME J. Appl. Mech.* **1933**, *55*, 39–44. [CrossRef]
8. Howland, R.C.J.; Knight, R.C. Stress functions for a plate containing groups of circular holes. *Philos. Trans. R. Soc. A* **1939**, *238*, 357–392.
9. Xu, X.; Fallahi, N.; Yang, H. Efficient CUF-based FEM analysis of thin-wall structures with Lagrange polynomial expansion. *Mech. Adv. Mater. Struct.* **2020**, *29*, 1316–1337. [CrossRef]
10. Xu, X.; Yang, H. Vision Measurement of Tunnel Structures with Robust Modelling and Deep Learning Algorithms. *Sensors* **2020**, *20*, 4945. [CrossRef] [PubMed]
11. Xu, X.; Shi, P.; Zhou, X.; Liu, W.; Yang, H.; Wang, T.; Yan, M.; Fan, W. A novel vision measurement system for health monitoring of tunnel structures. *Mech. Adv. Mater. Struct.* **2020**, *29*, 2208–2218. [CrossRef]
12. Xie, P.; Ma, S.K.; Wen, H.J.; Li, L.Y.; Jie, S.L.; Li, R.B. Theoretical analysis on stress distribution characteristics around a shallow buried cylinder Karst cave containing filling in limestone strata. *Arab. J. Geosci.* **2022**, *15*, 224. [CrossRef]
13. Xie, P.; Ma, S.K.; Wen, H.J.; Li, L.Y. Theoretical analysis on stress distribution characteristics around a shallow buried spherical Karst cave containing fill materials in limestone strata. *Environ. Earth Sci.* **2022**, *81*, 97. [CrossRef]
14. Zhao, H.; Xiao, Y.; Zhao, M.H.; Yang, C.W. Stability assessment method for subgrade with underlying rectangular cavity. *China J. Highw. Transp.* **2018**, *31*, 165–180.
15. Xie, P.; Wen, H.J.; Ma, S.K.; Yue, Z.R.; Li, L.Y.; Liu, J.F.; Li, R.B.; Cui, J. The bearing capacity analysis of limestone strata roof containing a shallow buried cylinder Karst cave. *Mech. Adv. Mater. Struct.* **2021**, 1–8. [CrossRef]
16. Lei, Y.; Deng, J.Z.; Liu, Z.Y.; Li, J.J.; Zou, G. A method to calculate ultimate bearing capacity of rock foundation with cavities considering load position offset. *Rock Soil Mech.* **2020**, *41*, 3326–3332. (In Chinese)
17. Keawsawasvong, S.; Ukritchon, B. Undrained stability of a spherical cavity in cohesive soils using finite element limit analysis. *J. Rock Mech. Geotech. Eng.* **2019**, *11*, 1274–1285. [CrossRef]
18. Keawsawasvong, S.; Ukritchon, B. Design equation for stability of shallow unlined circular tunnels in Hoek-Brown rock masses. *Bull. Eng. Geol. Environ.* **2020**, *79*, 4167–4190. [CrossRef]
19. Keawsawasvong, S. Limit analysis solutions for spherical cavities in sandy soils under overloading. *Innov. Infrastruct. Solut.* **2021**, *6*, 33. [CrossRef]
20. Keawsawasvong, S.; Shiau, J. Stability of Spherical Cavity in Hoek–Brown Rock Mass. *Rock Mech. Rock Eng.* **2022**, 1–12. [CrossRef]
21. Timoshenko, S.; Goodier, J.N. *Theory of Elasticity*; Xu, Z.; Wu, Y., Translators; Higher Education Press: Beijing, China, 1965.